

# Modeling extended contacts for nanotube and graphene devices

Norbert Nemec

*TCM Group, Cavendish Laboratory, 19 JJ Thomson Avenue, Cambridge CB3 0HE, UK. and  
Institute for Theoretical Physics, University of Regensburg, D-93040 Regensburg, Germany*

David Tománek

*Physics and Astronomy Department, Michigan State University, East Lansing, MI 48824-2320, USA. and  
Institute for Theoretical Physics, University of Regensburg, D-93040 Regensburg, Germany*

Gianaurelio Cuniberti

*Max Bergmann Center for Biomaterials, Dresden University of Technology, D-01062 Dresden, Germany. and  
Institute for Theoretical Physics, University of Regensburg, D-93040 Regensburg, Germany*

(Dated: October 28, 2018)

Carrier injection into carbon nanotubes and graphene nanoribbons, contacted by a metal coating over an arbitrary length, is studied by various means: Minimal models allow for exact analytic solutions which can be transferred to the original system with high precision. Microscopic *ab initio* calculations of the electronic structure at the carbon-metal interface allow us to extract—for Ti and Pd as contacting materials—realistic parameters, which are then used in large scale tight-binding models for transport calculations. The results are shown to be robust against nonepitaxially grown electrodes and general disorder at the interface, as well as various refinements of the model.

PACS numbers: 73.40.Cg, 73.63.Rt, 81.05.Uw

## I. INTRODUCTION

The high electrical conductivity of metallic carbon nanotubes (CNTs) can be attained, thanks to a unique combination of several features. The quasi-one-dimensional crystal structure, together with a low density of defects, allows us to explore the theoretical limit of conductance of  $4e^2/h$  at the charge neutrality point. The stiffness of carbon-carbon bonds reduces the effect of electron-phonon coupling at room temperature.<sup>1</sup> Also, restricting electron movement to a single dimension results in a very small phase space, which strongly reduces the effectiveness of scattering. A further reduction of backscattering is caused by the low density of states at the Fermi energy in combination with a high Fermi velocity. Considering all these factors, measured ballistic lengths of several microns<sup>2</sup> become understandable. Yet, to exploit the potential for carrying current densities of up to  $10^9$  A/cm<sup>2</sup>,<sup>3</sup> the contacts at a nanometer scale become crucial.

For graphene, which has been shown to allow ballistic transport over similar lengths,<sup>4</sup> the contacts play an equally important role.<sup>5</sup> Finite-width graphene nanoribbons (GNRs) are discussed as nanoelectronic devices and interconnects, showing both similarities and distinctive differences when compared to nanotubes. With first experimental results becoming available,<sup>6</sup> many of the theoretical predictions about GNRs will soon be put to test.<sup>7,8,9,10</sup>

Experimentally, a crucial factor for obtaining good metallic contacts are the wetting properties of the material. Thus, it has been observed that Ti, Ni and Pd form continuous coatings on single-wall CNTs while Au, Al and Fe form isolated particles.<sup>11</sup> Furthermore,

among several common contact metals, Ti was found to be the only one where true chemical bonds could be observed, while the others showed only weak van der Waals interactions.<sup>12</sup> Surprisingly enough, Pd—traditionally known as a rather poor conductor—was found to form better and more reliable Ohmic contacts for CNTs than Ti<sup>2</sup> and could be successfully applied to produce a CNT field effect transistor with Ohmic contacts.<sup>13</sup> It is generally believed that this superiority of Pd is due to its high work function ( $\phi_{\text{Pd}} = 5.1$  eV) that matches well with that of CNTs [e.g.,  $\phi_{(7,0)} \text{ CNT} = 5.1$  eV (Ref. 14)] and thereby avoids a high Schottky barrier. Pt, which has an even higher work function, would therefore be expected to perform even better as a contacting material, but as it turns out it does not form Ohmic contacts at all.<sup>15</sup>

A further experimental puzzle is the question of the effective length of contacts formed by a coating metal layer: While some studies report that transport occurs

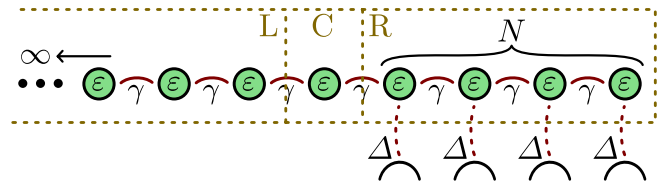


FIG. 1: (Color online) Minimal model for extended contacts solvable analytically: a linear chain of identical atoms (one orbital per atom) with hopping integral  $\gamma$  between nearest neighbors. To the left, the chain continues infinitely; at the right end,  $N$  atoms are contacted, each by an independent wideband lead of strength  $\Delta$ . For defining the transmission, the system is virtually split into three regions: the conductor  $C$  and the leads  $L$  and  $R$ .

only at the edge of the contact,<sup>2</sup> others state that the contact resistance depends on the length of the contact<sup>16</sup> or that extended contacts show a clearly distinct behavior from pointlike contacts.<sup>17</sup>

Various theoretical studies have been conducted to investigate these issues: In *ab initio* studies comparing Au, Pd and Pt contacting an (8, 0) CNT, Pd was found to have the lowest Schottky barrier.<sup>18</sup> Another *ab initio* study comparing the metal-graphene bonding of the same three metals indicated a very small binding energy for Au. For Pd it is somewhat larger, while for Pt the bonding is yet stronger.<sup>19</sup> The bad contacts formed by Pt are here attributed to a clustering effect of larger metal grains. Direct *ab initio* simulations of transport in a metal-contacted CNT compared Pd and Au,<sup>20,21</sup> finding again that Pd forms superior contacts. Ti was also found to form strong bonds to a nanotube surface<sup>22</sup> and to form superior point contacts for CNTs.<sup>23</sup>

Apart from these practical issues in explaining and improving the quality of materials, the study of contact models is also of great theoretical relevance: In studying the physics of electronic devices at the nanometer scale, it is generally crucial to have detailed control over the contacts.<sup>24,25</sup> Indeed, specifying properties of nanoelectronic devices is generally completely meaningless without clearly stating the way the system was contacted or—for theoretical studies—how the contact was modeled.

In a previous work,<sup>26</sup> we have demonstrated the counterintuitive finding that the optimal transparency in extended contacts for CNTs is achieved not by strong chemical bonding—as it would be the case for pointlike contacts<sup>23,27,28,29</sup>—but rather by contact materials that gently couple to the tube surface, allowing us to exploit the length of the tube-metal interface to smoothly inject the electrons with minimal reflection at the contact.

In this paper, we will present a detailed analysis of the model used for our previous findings. A minimal model, reducing the CNT or GNR to a single atomic chain and considering a semi-infinite wire with only a single contact at one end, allows an analytic solution that gives detailed insight in the mechanism of an extended contact (see Fig. 1). The results from this model have a close relation to the physics of Breit-Wigner resonances, which will be briefly sketched out at the beginning. After a thorough analysis of the minimal model, we will demonstrate how the results can be transferred to more realistic structures and explain in detail how the missing parameters could be quantitatively estimated from *ab initio* calculations of Pd and Ti as two typical contacting materials.

## II. BREIT-WIGNER RESONANCE

The conductance for a molecular junction, consisting of a single energy level  $\varepsilon$  in a two-terminal setup between two leads, is given in terms of the left and right tunneling

rates  $\Gamma_L$  and  $\Gamma_R$  by the Breit-Wigner equation<sup>30,31,32</sup>

$$G(E) = \frac{2e^2}{h} \frac{\Gamma_L \Gamma_R}{(E - \varepsilon)^2 + (\Gamma_L + \Gamma_R)^2 / 4}. \quad (1)$$

The bell-shaped peak in this expression as a function of the energy is well known. What is rarely noted in literature, however, is the fact that also for fixed energy  $E$  and one fixed contact  $\Gamma_L$ , the conductance as a function of the other contact  $G(\Gamma_R)$  has a bell shape with an optimum at the balanced coupling  $\Gamma_R = \Gamma_L$ . A new perspective to this old issue was provided in the recent experiments by Grüter et al.<sup>33</sup> Small couplings ( $\Gamma_R \ll \Gamma_L$ ) result in a linear  $\Gamma_R$  dependence of the conductance typical of tunneling phenomena, while for large coupling ( $\Gamma_R \gg \Gamma_L$ ), such better contact  $\Gamma_R$  results in an overall suppressed conductance. One way to understand this counterintuitive behavior is to consider the tunneling rate  $\Gamma$  as a measure for the chemical bond between the conducting orbitals of the molecule and the lead: A strong bond to one of the leads causes the molecule itself to virtually become part of that lead so that we observe the physics of a single point contact. Furthermore, the strong bonding results in a strong redistribution of the spectral weight of the energy level in the molecule, i.e., in a low local density of states (LDOS) at the energy  $\varepsilon$ . The tunneling conductance, which directly probes this LDOS, will therefore be suppressed by large  $\Gamma_R$ .

Once the length  $N$  of a contact is increased for an extended molecule, the optimal value decreases monotonically with the number of contact points  $N$ , as displayed in Fig. 2. As will be shown later [see Eq. (7)] this value scales like  $\Gamma_R = \Gamma_L \ln N/N$  for large  $N$ .

## III. ANALYTICAL MODEL

A minimal model that captures the essential physics of extended contacts is set up as follows. The CNT or GNR is represented by a linear chain of atoms with the hopping integral  $\gamma$  and the onsite energy  $\varepsilon = 0$  (fixing the energy offset). A two-probe setup is defined by selecting an arbitrary single electron as the “conductor” and the semi-infinite sections at both ends as “leads”. In this unmodified setup, the system is fully transparent, so the transmission  $T(E)$  is equal to the number of channels  $N_{\text{ch}}$  at any given energy. The single cosine-shaped band of the linear chain provides a single transmission channel

$$T_{\text{band}}(E) = \Theta(E + 2\gamma) \Theta(-E - 2\gamma)$$

which presents a theoretical upper transmission limit when scattering at the contacts could be neglected.

An “extended contact” to the linear chain is now modeled by replacing the semi-infinite lead by a finite  $N$ -atom chain contacted in each atom individually by a wideband lead of strength  $\Delta$ . (For a sketch of the model, see Fig. 1.) A full solution of this model is obtained by calculating

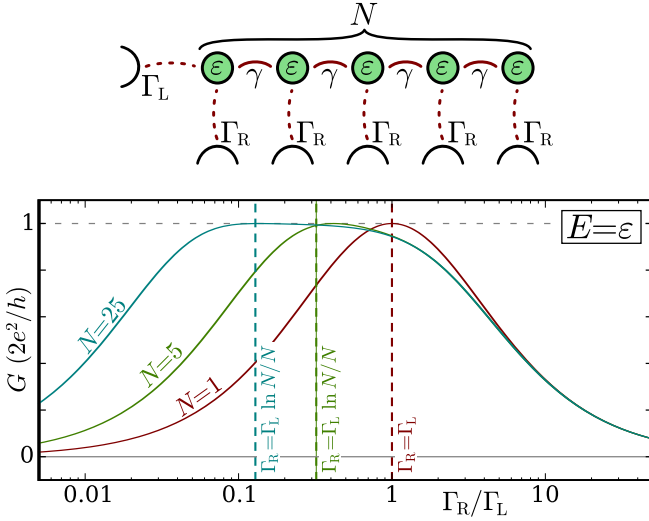


FIG. 2: (Color online) Breit-Wigner resonance in the conductance of an extended molecule sandwiched between two leads. The internal hopping is fixed as  $2\gamma = \Gamma_L$  to allow an optimal match to the left contact. In the case  $N = 1$ , the system is identical to the molecular junction described by Eq. (1). The transmission shows the shift of the Breit-Wigner peak towards lower  $\Gamma_R$  with growing  $N$ . The functional form of this shift can be approximated for large  $N$  as  $\Gamma_R = \Gamma_L \ln N/N$  [see Eq. (7)].

the conductance as the quantum mechanical transmission probability,

$$G(E) = \frac{2e^2}{h} T(E).$$

This can be done within the Landauer approach to transport by means of the Green function formalism, as shown in the Appendix. As a result, one obtains (for  $\varepsilon = 0$ )

$$T(E) = \frac{8\sqrt{4 - E^2/\gamma^2} \text{Im}[f_N(E/2\gamma - i\Delta/4\gamma)]}{\left| E/\gamma - i\sqrt{4 - E^2/\gamma^2} - 2f_N(E/2\gamma - i\Delta/4\gamma) \right|^2},$$

with  $f_N(x) = U_{N-1}(x)/U_N(x)$ .  $U_N(x)$  are the Chebyshev polynomials of the second kind, as given in Eq. (A4). To gain a full understanding of the physics described by this expression, the transmission  $T(E)$  is plotted as a function of the energy for different values of the two parameters  $N$  and  $\Delta$  (i.e., the length and the quality of the contact region) in Fig. 3. Two regimes can be identified: An *N-resonant* regime for low  $\Delta$ /small  $N$ , where the transmission shows about as many peaks as there are atoms in the contact region, and an *N-independent* regime for high  $\Delta$ /large  $N$ , where the transmission shows no resonances and depends only on  $\Delta$ .

The two different plots in Fig. 3 illustrate two aspects: For fixed  $N$  with increasing  $\Delta$ , the transparency of the system improves, goes through an optimum point, and degrades again, while for fixed  $\Delta$ , the transparency improves with growing  $N$  and saturates at an

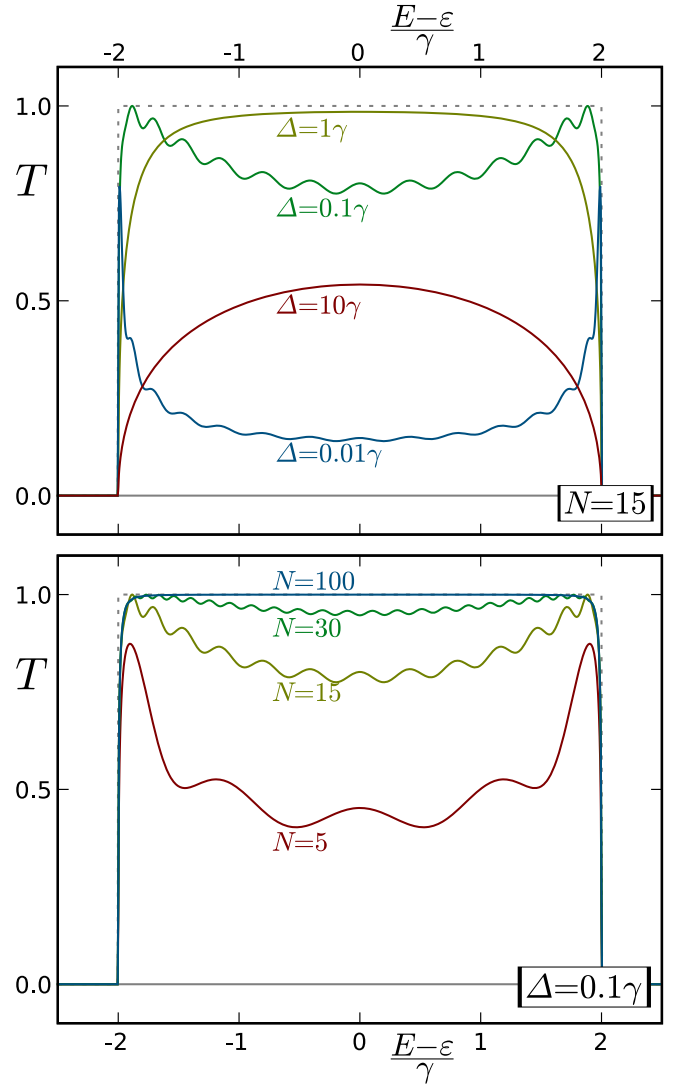


FIG. 3: (Color online) Transmission through the system displayed in Fig. 1, as given in Eq. (A8). Top panel: for a fixed contact length  $N$ , starting from low  $\Delta$ , the transmission first improves, reaches an optimum, and then degrades again at high  $\Delta$ . Bottom panel: For fixed contact strength  $\Delta$ , transmission improves with growing  $N$  and saturates for large  $N$ .

*N*-independent optimum. In both cases, the transmission goes through the two different regimes.

Especially the last point can be seen more clearly by looking at the reflection  $R = 1 - T$  in the energy range of the single channel of our system,

$$R = \left| \frac{E + i\sqrt{4\gamma^2 - E^2} - 2\gamma f_N(E/2\gamma - i\Delta/4\gamma)}{E - i\sqrt{4\gamma^2 - E^2} - 2\gamma f_N(E/2\gamma - i\Delta/4\gamma)} \right|^2 \quad (2)$$

In Fig. 4, this observable is plotted in a logarithmic scale, illustrating that the average value of the transmission already saturates at  $N = 100$  (specifically for  $\Delta = 0.1\gamma$ ). For larger values of  $N$ , the overall transparency is not improved any further, but the *N*-dependent resonances are smoothed out.

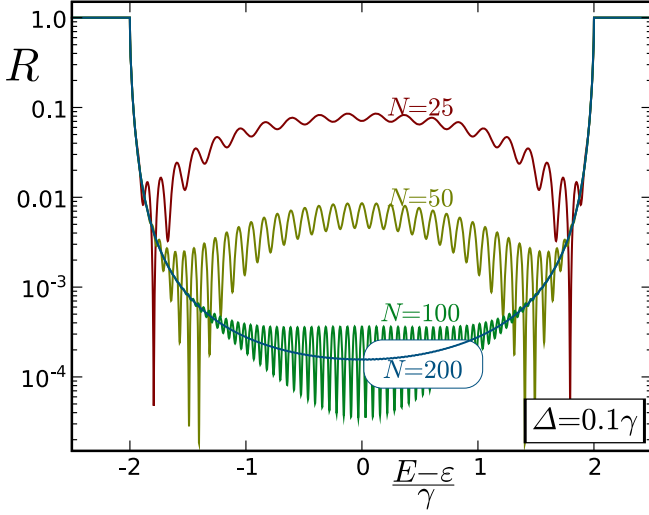


FIG. 4: (Color online) Contact reflection in the system displayed in Fig. 1, as given in Eq. (2). At fixed contact strength  $\Delta$ , with growing  $N$ , the contact becomes more transparent and saturates at an  $N$ -independent value.

To better understand the origin of this saturation, we fix the energy to the half filling case  $E = \varepsilon$  and study the transmission and the reflection for varying contact lengths  $N$  (see Fig. 5):

$$R(E = \varepsilon) = \left| \frac{1 + if_N(-i\Delta/4\gamma)}{1 - if_N(-i\Delta/4\gamma)} \right|^2. \quad (3)$$

Similar data were numerically obtained before for CNTs.<sup>34</sup> A different insight, however, can be gained from the reflection in a logarithmic scale: Ignoring the even-odd oscillations in  $N$ , one observes first an exponential decay of  $R$  with increasing  $N$ , followed by an abrupt crossover to an  $N$ -independent value. Both the rate of decay and the saturation value depend on  $\Delta$  in such a way that for lower values of  $\Delta$ , the transparency initially improves more slowly with the contact length, but ultimately  $R$  saturates at a lower value, which means higher contact transparency. This result, which we presented before based on numerical calculations on CNTs,<sup>26</sup> will be studied in more detail in the following using our analytical expressions.

An expression for the  $N$ -independent regime can easily be obtained as the limit  $N \rightarrow \infty$  of Eq. (A6) as

$$\begin{aligned} R_{N \rightarrow \infty}^{E=\varepsilon} &= \left| \frac{1 + if_{\infty}(-i\Delta/4\gamma)}{1 - if_{\infty}(-i\Delta/4\gamma)} \right|^2 \\ &= \left( \frac{\sqrt{\Delta^2/4 + 4\gamma^2} - \Delta/2 - 2\gamma}{\sqrt{\Delta^2/4 + 4\gamma^2} - \Delta/2 + 2\gamma} \right)^2, \end{aligned} \quad (4)$$

which can be further simplified for  $\Delta \ll \gamma$  to obtain

$$R_{N \rightarrow \infty, \Delta \ll \gamma}^{E=\varepsilon} = \frac{\Delta^2}{64\gamma^2}.$$

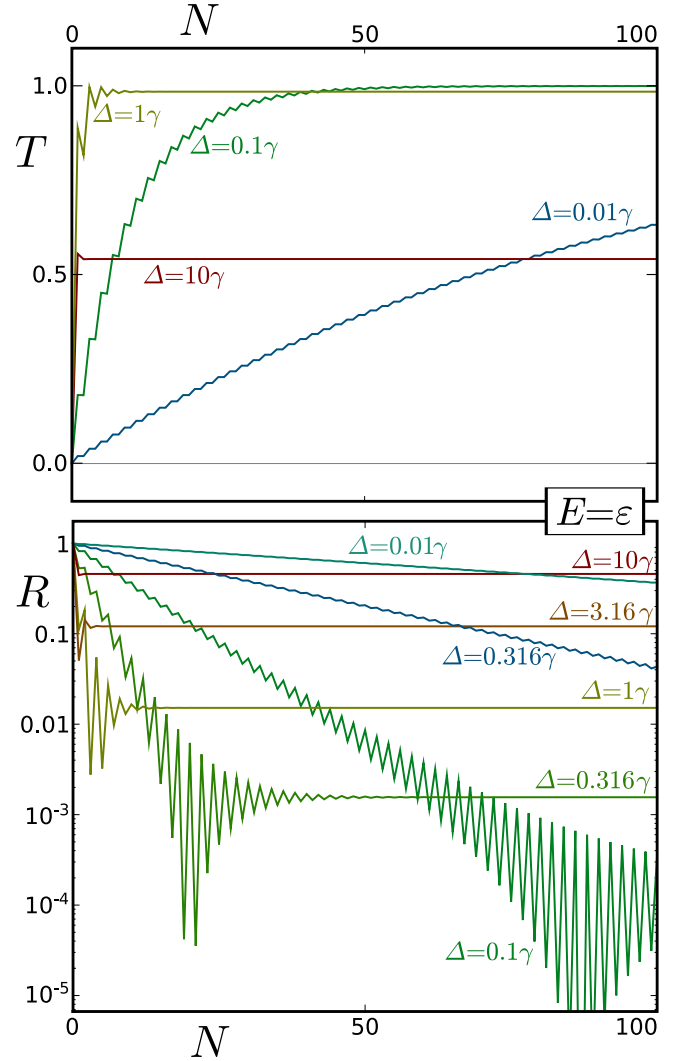


FIG. 5: (Color online) Transmission  $T$  (top panel) and contact reflection  $R$  (bottom panel) in the system displayed in Fig. 1 at fixed energy  $E = \varepsilon$  for varying contact length  $N$  and selected values of the contact strength  $\Delta$ .

The validity of this approximation is illustrated in Fig. 6.

The approach for finding the corresponding approximation for the  $N$ -resonant regime is less rigorous since a simple limit is not sufficient to capture the behavior in this case. A far better approximation is found graphically: The straight section in a semilogarithmic scale plot (inset of Fig. 6) indicates a clean exponential law. The missing coefficients are easily found from a Taylor expansion in  $\Delta = 0$ , yielding

$$\begin{aligned} R_{\text{resonant}}^{N \text{ even}} &= \exp(-N\Delta/\gamma), \\ R_{\text{resonant}}^{N \text{ odd}} &= \exp[-(N+1)\Delta/\gamma], \end{aligned}$$

both of which can be seen to fit precisely over the whole  $N$ -resonant region.

Having found good approximations for both regimes, the last missing piece is the crossover. For even  $N$ , the smooth shape of the crossover in Fig. 6 suggests a simple

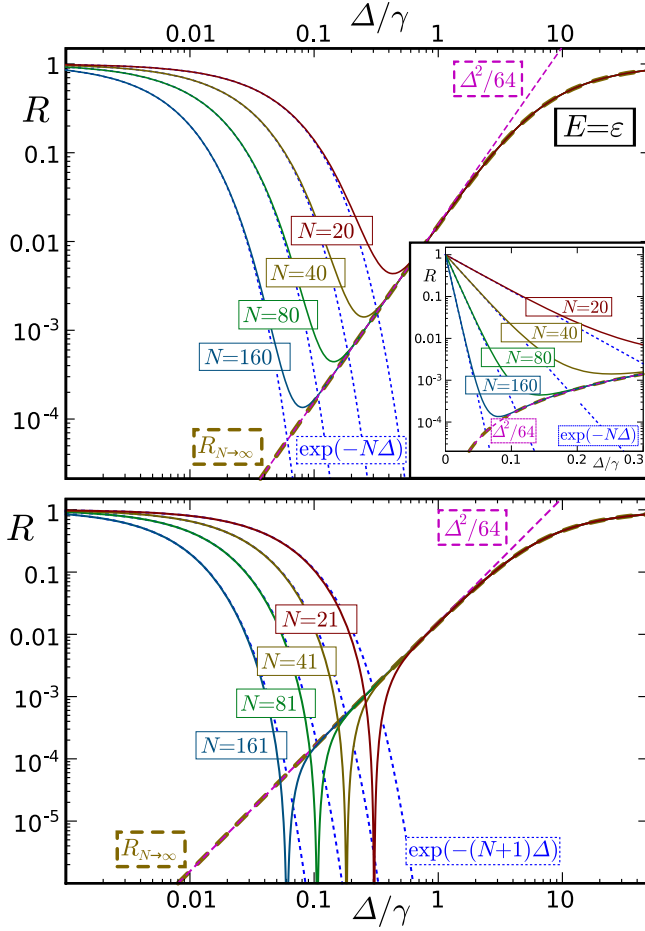


FIG. 6: (Color online)  $\Delta$  dependence of the contact reflection  $R$  for various even (upper panel) and odd (lower panel) contact lengths  $N$ . Solid: the exact value as given in Eq. (2). Dashed: the limit  $R_{N \rightarrow \infty}$  given in Eq. (4), along with its approximation  $\Delta^2/64\gamma^2$ , valid for  $\Delta \ll 1$ . Dotted: the approximation  $\exp(-N\Delta/\gamma)$ , valid for even  $N$  in the  $N$ -resonant regime. The inset shows the identical data in the semilogarithmic scale, further illustrating the precision of the  $\exp(-N\Delta/\gamma)$  approximation in the  $N$ -resonant regime.

function of the form  $R = \sqrt[n]{A^n + B^n}$  and, indeed, we find that for the case  $n = 1/2$ ,

$$R_{\text{crossover}}^N = \left( \sqrt{R_{N \rightarrow \infty}} + \sqrt{R_{\text{resonant}}^N} \right)^2 \quad (5)$$

gives an extremely good match over the full range of  $\Delta$ . Moreover, a very similar function is found to match the crossover for odd values of  $N$ ,

$$R_{\text{crossover}}^N = \left( \sqrt{R_{N \rightarrow \infty}} - \sqrt{R_{\text{resonant}}^N} \right)^2.$$

Both approximations show slight deviations from the exact value for small  $N$  but match with high precision for larger  $N$ . Obviously, the two reflection probabilities behave like squares of quantum mechanical amplitudes in-

terfering either constructively or destructively with each other.

The parameter values where  $R_{\text{resonant}}$  and  $R_{N \rightarrow \infty}$  coincide are of special interest. In the case that  $N \gg 1$ , where this coincidence happens for  $\Delta \ll \gamma$ , the condition for this is simply

$$\exp(-N\Delta/\gamma) = \Delta^2/64\gamma^2,$$

leading to an expression for the  $\Delta$ -dependent effective contact length

$$N_{\text{eff}}(\Delta) = \frac{2\gamma}{\Delta} \ln \left( \frac{8\gamma}{\Delta} \right), \quad (6)$$

over which a longer contact does not further modify transport. This can be interpreted as the length that contributes to the electron transmission for a very long contact.

The inverse of Eq. (6) can be expressed using the Lambert- $W$  function,<sup>35</sup>

$$\Delta_{\text{opt}}(N) = 2\gamma W(4N)/N$$

which can be approximated in the range of interest as

$$\Delta_{\text{opt}}(N) \approx 2\gamma \ln N/N. \quad (7)$$

#### A. Generalization to arbitrary injection energies

Having found the transport relations at the fixed energy  $E = \varepsilon$ , we can now continue with generalizing the results for  $E \neq \varepsilon$ . Assuming the general functional form of the reflection

$$R_{\text{resonant}} = \exp(-2N\Delta/\alpha_1) \\ R_{N \rightarrow \infty} = \Delta^2/\alpha_2^2,$$

we numerically find the following:

$$\alpha_1 = \sqrt{4\gamma^2 - E^2} (1 + \zeta),$$

which holds for arbitrary fixed  $N$  with an approximate error estimate  $|\zeta| \lesssim 1/N$  capturing the resonant oscillations. Considering the characteristic form of the density of states of the linear chain,

$$\rho(E) = \left( \pi \sqrt{4\gamma^2 - E^2} \right)^{-1},$$

we can rewrite the last expression as

$$\alpha_1 \approx 1/\pi\rho,$$

reflecting the similarity to a weak point contact where the tunneling transmission is proportional to the density of states on either side. The last relation could be confirmed numerically to hold very generally, as will be discussed below in the discussion of realistic contacts for nanotubes and ribbons.



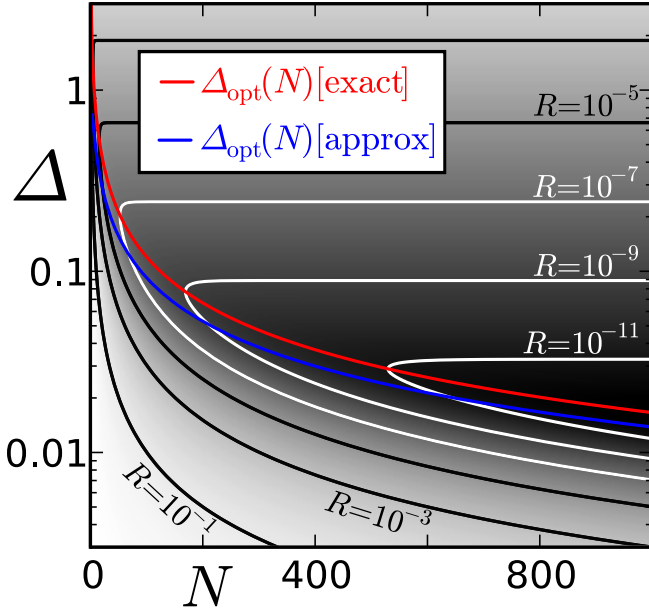


FIG. 7: (Color online) The contact reflection for even  $N$  obtained from Eq. (5). Quite visible are the two regimes separated by the minimal line  $\Delta_{\text{opt}}(N)$ . The “exact” value for  $\Delta_{\text{opt}}$  is the true minimum for fixed  $N$ . The “approximate” value comes from Eq. (7).

For the regime of  $N \rightarrow \infty$ , we can similarly, i.e. numerically, find the expression

$$\alpha_2 = \frac{2}{\gamma} (4\gamma^2 - E^2),$$

which fits the exact formula [Eq. (2)] with arbitrary precision for fixed  $\Delta \ll \gamma$  small enough and for  $E$  not too near the band edges. Unlike the formula for  $\alpha_1$ , however, expressing  $\alpha_2$  as a function of the density of states alone does not help to generalize the relation to other structures.

The crossover region, generally governed by interference effects, can be approximated by averaging over quantum mechanical phases, resulting in

$$R_{\text{crossover}} = R_{N \rightarrow \infty} + R_{\text{resonant}},$$

which gives a good approximation for the full parameter space with  $N \gg 1$ ,  $\Delta \ll \gamma$  and  $E$  away from band edges. Apart from the resonant oscillations, this now allows the full description of the reflection, and we find a precise numerical confirmation of the previously obtained expression of the effective contact length,

$$N_{\text{eff}}(\Delta) = \frac{1}{\pi\rho\Delta} \ln \frac{8\gamma^2 - 2E^2}{\gamma\Delta}.$$

A complete overview of the contact reflection and both parameters  $N$  and  $\Delta$  is shown in Fig. 7.

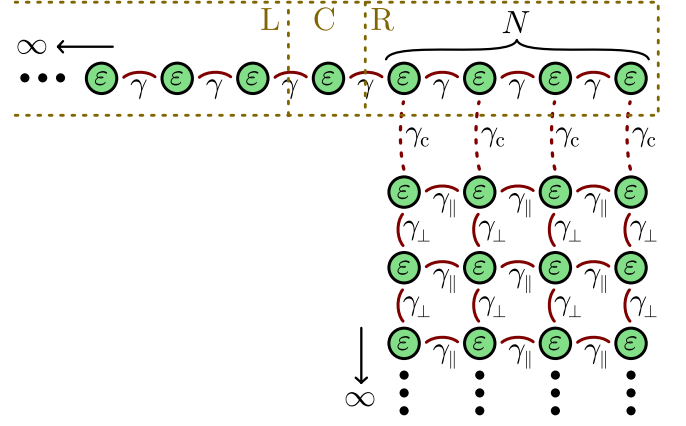


FIG. 8: (Color online) Generalized model including nondiagonal terms: the individual wideband leads for each atom in the extended contact region are replaced by a metal with an internal structure, here modeled as a 2D-square lattice. The new parameters are  $\gamma_{\parallel}$  and  $\gamma_{\perp}$ , describing the internal hopping in the lattice parallel and perpendicular to the contact surface, as well as  $\gamma_c$ , describing the hopping at the contact. For simplicity, we consider only the isotropic case  $\gamma_{\parallel} = \gamma_{\perp}$ . This leaves us with the single effective parameter  $\Delta = \gamma_c^2/\gamma_{\perp}$ .

#### IV. NONDIAGONAL CONTACTS

To generalize our results beyond the diagonal contact approximation, we model the contacting metal not as a single-parameter wideband lead but as a material with an internal structure, leading to off-diagonal terms in the contact matrix (see Fig. 8). Figure 9 illustrates that the off-diagonal terms in the self-energy do not bring any qualitative changes to the behavior described before. An exact quantitative mapping would depend strongly on the details of the model.

#### V. REALISTIC CONTACTS FOR CARBON NANOSTRUCTURES

For the case of CNTs and GNRs, the method of the Chebyshev polynomials cannot be used to obtain an analytical solution due to the noncommutativity of the partial Hamiltonians of the periodic structure. In numerical studies, however, we find that the behavior is identical to that of the linear chain, except for a quantitative adjustment of the parameters  $\alpha_1$  and  $\alpha_2$  (see Fig. 10). The  $N$ -resonant regime can be described precisely by a simple generalization of the law found for the linear chain

$$R_{\text{resonant}} = \exp(-2N\Delta/\alpha_1),$$

$$\alpha_1 = N_{\text{ch}}/\pi\rho,$$

where  $N_{\text{ch}}$  is the number of channels and  $\rho$  the total density of states per unit cell. Generally, both values are dependent on the energy and the chirality of the tube or width and edge geometry of the ribbon. For metallic

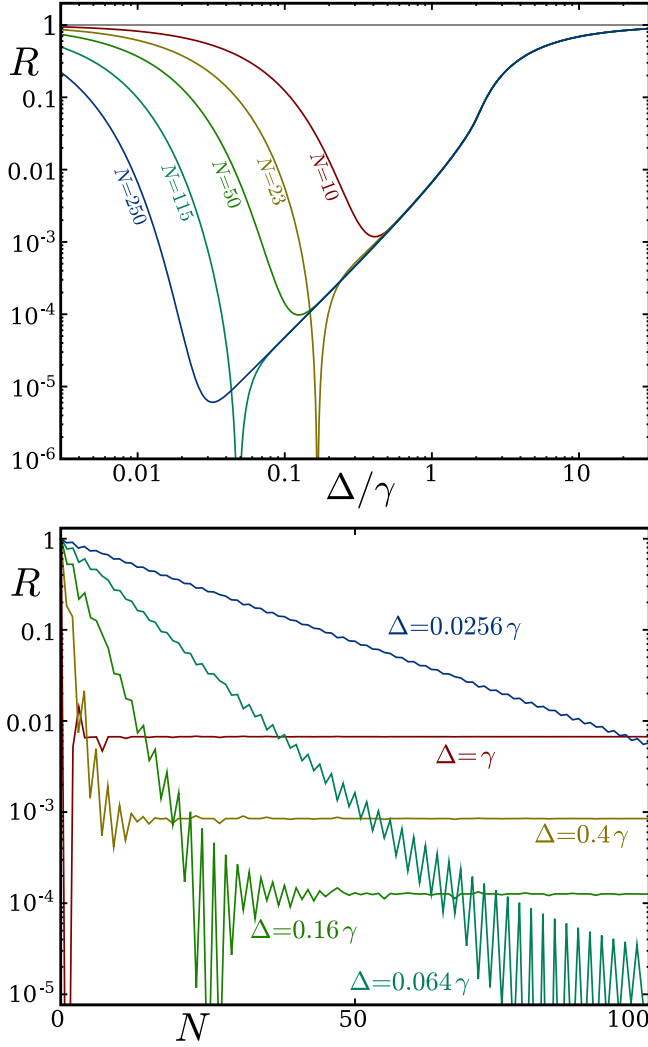


FIG. 9: (Color online) Nondiagonal contacts: Reflection  $R$  of the generalized model displayed in Fig. 8. Relating the parameter  $\Delta = \gamma_c^2/\gamma_\perp$  to the parameter  $\Delta$  of the wideband leads, the results are qualitatively similar to those of the original model (Figs. 5 and 6). One prominent difference is the enlarged reflection  $R(\Delta)$  for  $\Delta/\gamma$  between 1 and 10: While the diagonal self-energy was uniform for every atom along the contact, the nondiagonal self-energy now is sensitive to the edge of the contact. For large values of  $\Delta$ , where only the atoms near the edge contribute to the transport, this causes the visible deviation from the  $R = \Delta^2/\alpha_2^2$  law. The same reason is behind the visible irregularities in the resonant oscillations of  $R(N)$ .

CNTs near the Fermi energy, however, one finds the general values of  $N_{\text{ch}} = 2$ ,  $\rho = 2N_{\text{ch}}/3\gamma d_{\text{CC}}$ , and, therefore,  $\alpha_1 = 3\gamma d_{\text{CC}}/2\pi\ell_{\text{uc}}$ . ( $\gamma = 2.66$  eV and  $d_{\text{CC}} = 1.42$  Å). Introducing the physical length of the contact region  $L = \ell_{\text{uc}}N$  with the length of the unit cell  $\ell_{\text{uc}}$ , the previous formula can be rewritten as

$$R_{\text{resonant}} = \exp(-2L\Delta/\alpha_1\ell_{\text{uc}}), \\ \alpha_1\ell_{\text{uc}} = 1.80 \text{ eV Å}.$$

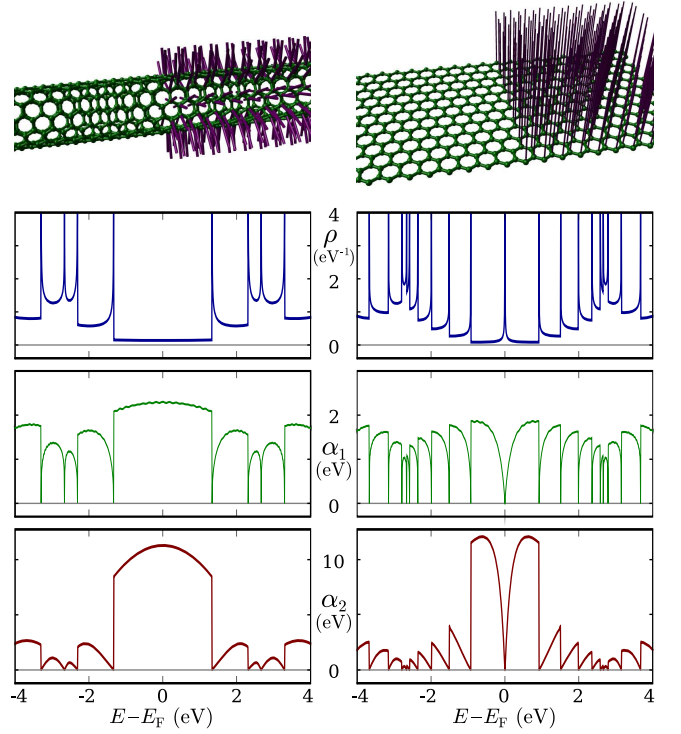


FIG. 10: (Color online) Extended contacts for a (6,6) CNT (left) and the corresponding graphene nanoribbon. Top panel: density of states with characteristic van Hove singularities. The zigzag-edge state in the nanoribbon causes a peak at  $E = E_F$ . Center panel: The value  $\alpha_1 = -2N\Delta/\ln R$ , here computed for  $N = 40$  and  $\Delta = 10^{-5}$  eV, lies already very near to the limiting case  $\alpha_1 = N_{\text{ch}}/\pi\rho$ . Bottom panel: The value  $\alpha_2 = \Delta/\sqrt{R}$  is well converged for  $N \rightarrow \infty$  and  $\Delta = 10^{-2}$  eV. Note the suppression of both  $\alpha_1$  and  $\alpha_2$  in the ribbon at  $E_F$  where the presence of the localized edge state suppresses the conductance in the contact region.

For the  $N$ -independent regime, the general law of  $R_{N \rightarrow \infty} = \Delta/\alpha_2$  still holds, but the functional form of the parameter  $\alpha_2$  at arbitrary energies could not be determined. Generally, it turns out that  $\alpha_2$  is suppressed at van Hove singularities in a similar way as  $\alpha_1$  is. Furthermore, metallic CNTs have a fairly constant value of  $\alpha_2$  around  $E_F$ . At  $E = E_F$ , we find  $\alpha_2 = 4.24\gamma$  for armchair CNTs and  $\alpha_2 = 5.66\gamma$  for metallic zigzag CNTs.

For GNRs, the situation is slightly more complex due to the presence of edge states at zigzag edges.<sup>7,8,10</sup> In metallic ribbons with armchair edges, the situation is similar to that of metallic CNTs, and we find a value of  $\alpha_2 = 8.0\gamma$  at  $E = E_F$ . The quantitative difference from the value of the corresponding CNTs can be explained by the presence of only one conduction channel at the Fermi energy. For ribbons with zigzag edges, however, our simplified model suggests that the constant  $\alpha_2$  is completely suppressed at  $E = E_F$  due to the peak in the density of states, caused by the edge state.

Physically, this suppressed value of both  $\alpha_1$  and  $\alpha_2$  suggests that the injection of charges into the edge state

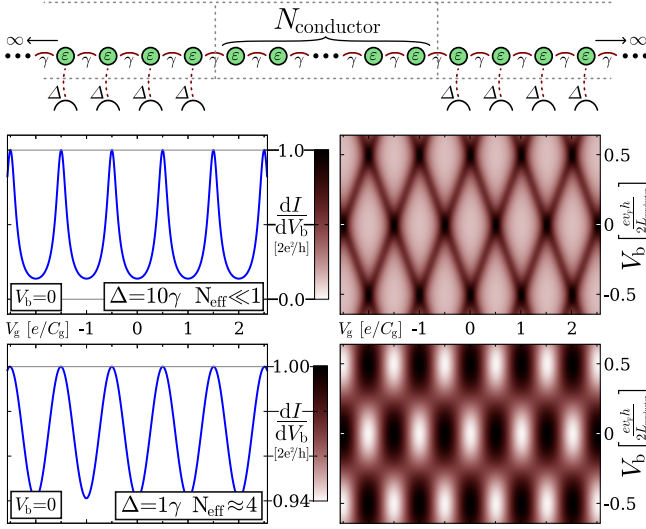


FIG. 11: (Color online) Differential conductance through a two-terminal setup of a linear chain with symmetric, infinite-length extended contacts. The central region consists of  $N_{\text{conductor}} = 200$  atoms. The distance between the Fabry-Pérot oscillations in the gate voltage  $V_g$  depends on the total gate capacitance  $C_g$  as  $\delta V_g = e/C_g$ . The extent of the diamonds in direction of the bias voltage  $V_b$  depends directly on the level spacing  $\delta E = v_F \hbar / 2L_{\text{conductor}} = 2\gamma\pi/N_{\text{conductor}}$  as  $\delta V_b = e\delta E$ . Top: strong coupling  $\Delta = 10\gamma$ , leading to an extremely short effective contact length producing sharp resonances and a distinct diamond pattern. Bottom: moderate coupling  $\Delta = 1\gamma$  leading to an effective contact length of about four unit cells. The oscillations have a sinoidal shape with strongly reduced amplitude. For yet weaker coupling as it is to be expected for Pd or Ti, the amplitude is rapidly reduced even further making the oscillations undetectable. In this case, a strong defect within the contact region may act as a point of scattering and recover sharp resonances.

via extended leads is less efficient than that into the conduction channels of nanotubes or armchair ribbons. However, taking into account the results of detailed *ab initio* calculations reveals a spin splitting of the edge states, which strongly affects the bands at the Fermi energy and opens special spin transport channels,<sup>10</sup> which are not captured by our model.

## VI. TWO-TERMINAL SETUP AND FABRY-PÉROT PHYSICS

A realistic setup for conduction measurements in CNTs and GNRs generally needs a second contact at the other end of the system to close a circuit. Such a setup is well known to lead to Fabry-Pérot-like oscillations of the conductance along the energy range.<sup>36</sup> For very bad contacts, Coulomb blockade has been observed, but we intentionally avoid this regime that would demand the inclusion of charging effects.

One important aspect of Fabry-Pérot oscillations is their experimental use in measuring the length of the

scattering region. In the zero-bias differential conductance, the spacing of the Fabry-Pérot resonances depends on the gate capacitance  $C_g$  alone as  $\delta V_g = e/C_g$ . Only the diamond shapes in a plot of the finite bias differential conductance

$$\frac{dI}{dV_b} = \frac{e^2}{h} \left[ T \left( \frac{V_g C_L}{e\rho} - \frac{eV_b}{2} \right) + T \left( \frac{V_g C_L}{e\rho} + \frac{eV_b}{2} \right) \right]$$

give access to the spacing of the energy levels  $\delta E = \hbar v_F / L_0$  and can thereby be used to measure the length  $L_0$  of the resonator.

As visible in Fig. 11, however, the amplitude of these oscillations is strongly reduced as soon as the effective contact length exceeds the length of one unit cell. One could view this situation as *smooth contacts* that cause the Fabry-Pérot oscillations to be broadened and the resonator length  $L_0$  to be ill defined.

In some experiments using extended contacts on CNTs, the length of the scattering regions was measured to be just as long as the uncovered region of the tube,<sup>2</sup> which could be explained based on our model by a strong contact  $\Delta$  and, therefore, a short effective contact length. For weaker contacts  $\Delta$ , it is to be expected that Fabry-Pérot oscillations cannot be cleanly observed any more. A point defect inside the contacted region might, of course, act as a scattering point instead and give rise to oscillations that indicate a resonator longer than the uncovered region of the CNT.

In our previous study,<sup>26</sup> we chose to average this oscillating conductance over  $E_F \pm 0.5\text{ eV}$  in order to separate the finite-length Fabry-Pérot effects from the effects caused by the contacts themselves. Physically, this is similar to the thermal effects caused by high enough temperature. For the chosen conductor length of  $L_0 = 100\text{ nm}$ , this approach was very successful in canceling all Fabry-Pérot oscillations and in reproducing the physics of a single extended contact. The resonance oscillations within the contact were, of course, also strongly suppressed by the averaging, leaving only a minimal signature that we correctly identified as such.

## VII. NONEPITAXIAL CONTACTS

Unlike the theoretical model contacts presented so far, realistic samples produced in experiment are never perfectly epitaxial but contain imperfections due to fabrication faults, lattice mismatch or metal faceting. To check whether the effects described so far are robust to such perturbations, we have investigated various kinds of disorder at the contact. A relatively weak disorder was implemented as random fluctuations of the contact parameter  $\Delta$  on each atom  $i$  as

$$\Delta_i^{\text{fluct}} = \Delta (1 + \xi_i^{\text{fluct}} W),$$

with an evenly distributed random variable  $-1 \leq \xi_i^{\text{fluct}} \leq 1$  and a parameter  $W$  specifying the relative strength of



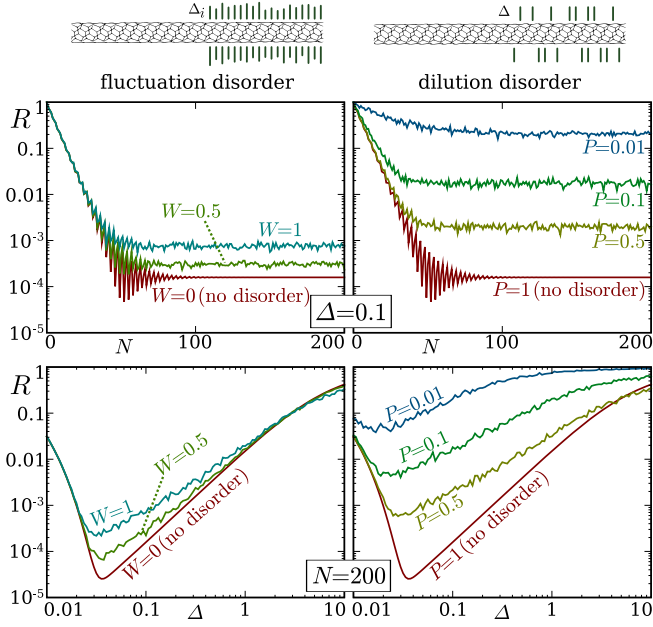


FIG. 12: (Color online) Effects of two different kinds of disorder on extended contacts: relatively weak *fluctuation disorder* with varying contact strength  $\Delta_i$  on each atom  $i$  and stronger *dilution disorder* with only a randomly selected fraction of the atoms in the contact region attached to a lead. In each case, the parameter  $\Delta$  refers to the *average* contact strength. For details, see the text.

the fluctuations. As can be seen in Fig. 12, even for the strongest possible value  $W = 1$ , the effect of the disorder is moderate and purely quantitative.

An even stronger disorder was realized by using a model of diluted contacts, where only a randomly selected fraction of the atoms in the contact region is contacted,

$$\Delta_i^{\text{diluted}} = \begin{cases} \Delta/P & \text{with probability } P \\ 0 & \text{with probability } 1 - P. \end{cases}$$

This kind of disorder modifies to the observed behavior to a much larger degree, but even in the extreme case of a 1% dilution (i.e.  $P = 0.01$ ), the general trend of the original model is well preserved (see Fig. 12).

### VIII. MATERIAL RELATED CALCULATIONS

To link the model results obtained so far to the physical properties of real contact materials, we performed density functional theory (DFT) calculations of Ti and Pd monolayers interacting with a graphene layer as described before.<sup>26</sup> We described the valence electrons by Troullier-Martins pseudopotentials and used the Perdew-Zunger form of the exchange-correlation functional in the local density approximation to DFT, as implemented in the SIESTA code.<sup>37</sup> With a double-zeta basis and a 100 Ry energy cutoff in the plane-wave expansions of the electron density and potential, we found the total energy to

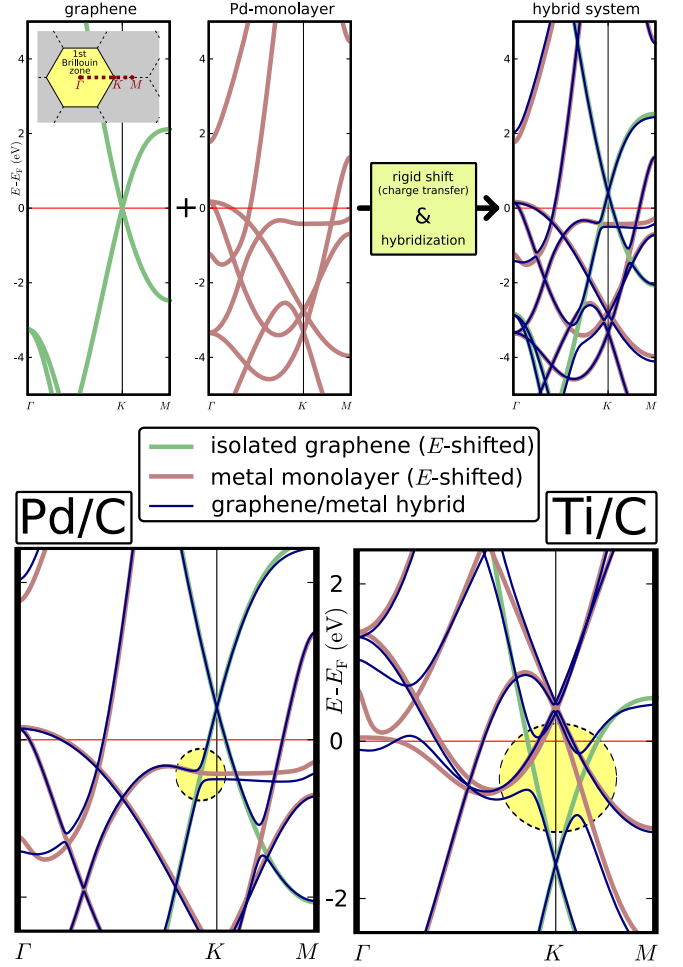


FIG. 13: (Color online) Analysis of the hybridization between a graphene sheet and a metal monolayer. As visible in the upper scheme, the hybrid band structure matches well with an overlay of the band structures of the two individual systems rigidly shifted in energy and hybridization at some band crossings. Highlighted in the Pd/C and Ti/C band structures are the regions of interest, i.e., those hybridizations that contribute most to the electron injection.

be converged to  $\lesssim 1\text{meV/atom}$ . We performed a full structure optimization to determine the equilibrium adsorption geometry, the adsorption energy, and the local charge redistribution caused by the metal-graphene interaction. Since the interatomic distances in bulk Pd (2.7 Å) and Ti (2.95 Å) lie close to the honeycomb spacing in graphene (2.46 Å), we considered only epitaxial adsorption. For both Pd and Ti, we found a slight preference for the sixfold hollow site on graphite. For Pd, we found the equilibrium interlayer distance to be 3.2 Å, consistent with a relatively weak, mostly covalent bond energy of 0.3 eV per Pd atom. The interaction between an epitaxial Ti monolayer and graphene was only insignificantly stronger with 0.4 eV per Ti atom at an interlayer distance of 3.0 Å.

To study the electronic coupling between the two sys-

tems, we first inspected the band structure (see Fig. 13). Especially for Pd as a contacting metal, the extraction of parameters for our model is greatly simplified by the fact that the band structure of hybrid lies close to the superposition of the metal and carbon band structures. One can see a rigid shift of the carbon bands by  $E_C = 0.374$  eV while the palladium bands are shifted slightly in the opposite direction with  $\Delta E_{\text{Pd}} = -0.020$  eV. On top of this rigid shift, one can observe slight hybridization effects in the band structure. For injecting conduction electrons into a graphene sheet or the wall of a carbon nanotube, the most important area of the Brillouin zone is the  $K$  point, the Fermi point of graphene. In Fig. 13, a small avoided crossing is visible near this region in the Pd/C band structure. To extract an estimate of tight-binding parameters from these data, we modeled a honeycomb lattice and a matching hexagonal lattice representing both sheets. As it turned out, a single orbital per atom is sufficient to obtain bands that can be fitted to the hybridizing bands near the Fermi level with a single parameter each. Now, an additional coupling between the two sheets was introduced, linking each Pd atom with its six neighboring C atoms. This hopping parameter could then be tuned to reproduce a hybridization between the two subsystems, which is close to that in the hybrid band-structure obtained from DFT, resulting in a coupling of  $t_{\text{Pd/C}} \approx 0.15$  eV.

For the case of Ti, the distortions in the band structure caused by the hybridization of the two layers are considerably stronger than for Pd. Still, the change in the carbon related levels can be modeled by a rigid shift of  $\Delta E_C = -1.15$  eV. To determine the hopping parameter, the same procedure as for Pd could not be directly applied, because the relevant band of the Ti-monolayer cannot be reproduced with a single-orbital hexagonal lattice. Instead, a rough estimate was obtained by visually comparing the bandstructures themselves where the avoided crossing near the  $K$ -point is at least twice as large as for Pd, giving an estimated value of  $t_{\text{Ti/C}} \gtrsim 0.3$  eV.

To turn these parameters into values of  $\Delta$  that can be directly placed into our model calculations, we need the surface density of states, which is comparable for both materials at  $\mathcal{N}_{\text{Me}} \approx 1$  eV<sup>-1</sup>. Finally, the connectivity at the interface is also important: Each C atom contacted to three different metal atoms simply triples the value of  $\Delta$ . The internal connections inside the metal are already taken into account with the surface density of states and do not have to be considered any further. With the relation  $\Delta = t^2 \mathcal{N}$ , this again gives rough estimates of  $\Delta_{\text{Pd}} \approx 0.06$  eV and  $\Delta_{\text{Ti}} \gtrsim 0.3$  eV.

Unfortunately, this approach of computing a graphene layer and a layer of the contacting material within a common unit cell cannot necessarily be transferred to other materials of interest in any straightforward way. There exist, however, *ab initio* calculations of various metals in contact with graphene or CNTs that show a clear trend.<sup>19,38,39</sup> The highly conducting metals Au, Ag and Cu generally have a very weak binding energy, insuffi-

cient for wetting the carbon surface; so, a clean contact is hard to achieve. Pd, Pt and Ti all have sufficient binding energies for wetting the surface. Pt and Ti both have higher binding energies than Pd. For pointlike end contacts, such strong bonds give good transparency.<sup>23</sup> For extended contacts, however, the weak bonds of Pd are to be preferred.

Previous calculations<sup>19</sup> attributed the difference between Ti and Pd metal contacts to the formation of different-sized metal clusters at the interface. Our results, presented above, offer a more fundamental explanation: It is exactly the weak bonding between Pd and graphene or CNTs—just large enough to wet the surface—that makes Pd such an excellent contact material.

## IX. CONCLUSIONS

To conclude, we introduced a model for electrical contacts for carbon nanotubes and graphene nanoribbons that captures the fact that the contacts in an experimental setup typically extend over a length of several tens of nanometers, covering the carbon structure with some contact metal. We have demonstrated the counterintuitive result that, given a metal coating of several nanometer length, the contact transparency is actually improved by using a metal that couples more weakly to the carbon surface. Using *ab initio* results of Ti and Pd as contact metals, we have demonstrated that Pd actually forms a weaker bond, giving an explanation of the experimental finding that Pd forms good contacts. This finding suggests a possible route for future attempts in optimizing the charge injection in carbon nanotubes and graphene, that is, to find contacting materials that couple to the carbon surface as softly as possible to exploit the available contact length.

Starting with a detailed analysis of an analytically solvable minimal model, we have demonstrated by numerical calculations that the qualitative results are robust to various modifications of the system. Replacing the atomic wire by the actual atomic structure of a carbon nanotube or a graphene ribbon can be accommodated by adjusting just two parameters at any given energy. Including a second contact to model a realistic two-terminal conductance measurement leads to Fabry-Pérot oscillations that can be averaged out to give the original result. A weak disorder in the contact interface has very little quantitative effect, and even a strong disorder (similar to metal grains forming contact only in certain points) leaves the qualitative behavior unchanged.

In view of a possible experimental confirmation of our results, the biggest challenge may lie in the fabrication of well-controlled finite-length contacts down below the magnitude of the effective contact length of a few nanometers. With current technology, this precision is yet out of reach, but with future developments, it should well be possible to tune the geometry of contact with

sufficient precision. An alternative approach would be to tune the coupling contact interface by some means. Direct tuning of the bonds, as it can be done for molecular junctions,<sup>33</sup> seems unfeasible for this kind of geometry. Instead, the insertion of an insulating atomic layer below the contacting metal is already being used to improve the contacts for graphene monolayers and might work as well for nanotubes.

### Acknowledgements

We acknowledge fruitful discussions with Ferdinand Evers, Sybille Gemming and Christian Schönenberger. This work was funded by the Volkswagen Foundation under Grant No. I/78 340 and by the European Union grant CARDEQ under Contract No. IST-021285-2. Support from the Vielberth Foundation is also gratefully acknowledged. D. T. acknowledges financial support by NSF NIRT Grant No. ECS-0506309, NSF NSEC Grant No. EEC-425826, and the Alexander von Humboldt Foundation.

## APPENDIX A: ANALYTICS FOR THE ONE-DIMENSIONAL MODEL

### 1. Transmission calculations

The Hamiltonian of a two-probe system for transport calculations is given by

$$\mathcal{H} = \begin{pmatrix} H_L & H_{Lc} & 0 \\ H_{cL} & H_c & H_{cR} \\ 0 & H_{Rc} & H_R \end{pmatrix} \quad (\text{A1})$$

where  $H_c$  describes the finite-size conductor region and  $H_{L/R}$  describes the leads, which are connected to independent reservoirs and have no direct contact with each other. From  $\mathcal{H} = \mathcal{H}^\dagger$  it follows that  $H_{Lc} = H_{cL}^\dagger$  and  $H_{Rc} = H_{cR}^\dagger$ .

To simplify the notation, we first define the *complex-energy Green function*:

$$\mathcal{G}(\mathcal{E}) = (\mathcal{E} - \mathcal{H})^{-1}$$

and derive from it the expressions for the retarded and advanced Green functions ( $\mathcal{E} = E \pm i\eta$ )

$$\begin{aligned} \mathcal{G}^r(E) &= \lim_{\eta \rightarrow 0^+} \mathcal{G}(E + i\eta), \\ \mathcal{G}^a(E) &= \lim_{\eta \rightarrow 0^+} \mathcal{G}(E - i\eta). \end{aligned}$$

The *transmission* through this system is given by<sup>40,41</sup>

$$T = \text{Tr} \{ \Gamma_L \mathcal{G}_c^r \Gamma_R \mathcal{G}_c^a \}, \quad (\text{A2})$$

with

$$\begin{aligned} \mathcal{G}_c &= (\mathcal{E} - H_c - \Sigma_L - \Sigma_R)^{-1}, \\ \Sigma_\alpha &= H_{c,\alpha} \mathcal{G}_\alpha H_{\alpha,c}, \quad \alpha = L, R, \\ \Gamma_\alpha &= i(\Sigma_\alpha^r - \Sigma_\alpha^a), \\ \mathcal{G}_\alpha &= (\mathcal{E} - H_\alpha)^{-1}. \end{aligned}$$

The Hamiltonian of the model at hand, depicted in Fig 1, can be split up according to Eq. (A1): The conductor consists of just one atom, so its Hamiltonian is a  $1 \times 1$  matrix  $H_c = (\varepsilon)$ . The left lead is a semi-infinite chain, contacted only at the last atom,

$$\begin{aligned} H_L &= \begin{pmatrix} \ddots & \ddots & \ddots & 0 \\ \dots & 0 & -\gamma & \varepsilon & -\gamma \\ & \dots & 0 & -\gamma & \varepsilon \end{pmatrix}_{\infty \times \infty}, \\ H_{cL} &= (\dots \quad 0 \quad 0 \quad -\gamma)_{1 \times \infty}. \end{aligned}$$

The right lead consists of a chain of  $N$  atoms, each attached to a wideband lead. This can be captured by defining an *effective Hamiltonian* of the form

$$H_R^{\text{eff}} = \begin{pmatrix} \varepsilon - \frac{i\Delta}{2} & -\gamma & \dots & 0 \\ -\gamma & \varepsilon - \frac{i\Delta}{2} & \ddots & \vdots \\ & -\gamma & \ddots & -\gamma \\ \vdots & & \ddots & \varepsilon - \frac{i\Delta}{2} & -\gamma \\ 0 & \dots & & -\gamma & \varepsilon - \frac{i\Delta}{2} \end{pmatrix}_{N \times N} \quad (\text{A3})$$

together with a contact point in the first atom only,

$$H_{cR} = (-\gamma \quad 0 \quad 0 \quad \dots \quad 0)_{1 \times N}.$$

Note that  $H_R^{\text{eff}}$  is the effective Hamiltonian containing the *retarded* self-energy, so  $\mathcal{G}_R^r = (E + i0^+ - H_R^{\text{eff}})^{-1}$  and  $\mathcal{G}_R^a = (E - i0^+ - (H_R^{\text{eff}})^\dagger)^{-1}$ .

In the following, we will simplify the notation by setting  $\gamma = 1$  and  $\varepsilon = 0$ . Both constants can be reintroduced in the final result [Eq. (A8)] by substituting  $E \rightarrow (E - \varepsilon)/\gamma$ .

### 2. Inverse based on Chebyshev polynomials

As a starting point for a full analytical solution, we look at a finite linear chain of length  $N$ , which has the Hamiltonian

$$\mathcal{H}^N = \begin{pmatrix} 0 & -1 & \dots & 0 \\ -1 & 0 & \ddots & \vdots \\ & -1 & \ddots & -1 \\ \vdots & & \ddots & 0 & -1 \\ 0 & \dots & & -1 & 0 \end{pmatrix}_{N \times N}.$$

The quantity of interest of this system is the 1,1 matrix element of the Green function  $\mathcal{G}^N(\mathcal{E}) = (\mathcal{E} - \mathcal{H}^N)^{-1}$ .

The solution is based on the Chebyshev polynomials of the second kind,<sup>42</sup> which can be defined via the determinant identity,

$$U_n(x) = \det \begin{pmatrix} 2x & 1 & & 0 \\ 1 & 2x & \ddots & \\ & 1 & \ddots & 1 \\ & & \ddots & 2x & 1 \\ 0 & & & 1 & 2x \end{pmatrix}_{n \times n},$$

or, equivalently, by the recursive definition,

$$\begin{aligned} U_0(x) &= 1, \\ U_1(x) &= 2x, \\ U_{n+1}(x) &= 2xU_n(x) - U_{n-1}(x). \end{aligned} \quad (\text{A4})$$

$$(A^{-1})_{ij} = \frac{1}{\det(A)} \det \begin{pmatrix} A_{1,1} & \cdots & A_{1,j-1} & 0 & A_{1,j+1} & \cdots & A_{1,N} \\ \vdots & \ddots & \vdots & \vdots & \vdots & \ddots & \vdots \\ A_{i-1,1} & \cdots & A_{i-1,j-1} & 0 & A_{i-1,j+1} & \cdots & A_{i-1,N} \\ 0 & \cdots & 0 & 1 & 0 & \cdots & 0 \\ A_{i+1,1} & \cdots & A_{i+1,j-1} & 0 & A_{i+1,j+1} & \cdots & A_{i+1,N} \\ \vdots & \ddots & \vdots & \vdots & \vdots & \ddots & \vdots \\ A_{N,1} & \cdots & A_{N,j-1} & 0 & A_{N,j+1} & \cdots & A_{N,N} \end{pmatrix}$$

to find

$$\begin{aligned} [\mathcal{G}^N(\mathcal{E})]_{i,j} &= [(\mathcal{E} - \mathcal{H}_N)^{-1}]_{i,j} \\ &= [\mathcal{G}^N(\mathcal{E})]_{j,i} \\ &\stackrel{i \leq j}{=} (-1)^{i-j} \frac{U_{i-1}(\mathcal{E}/2) U_{N-j}(\mathcal{E}/2)}{U_N(\mathcal{E}/2)} \end{aligned}$$

and, specifically,

$$\begin{aligned} [\mathcal{G}^N(\mathcal{E})]_{1,1} &= \frac{U_{N-1}(\mathcal{E}/2)}{U_N(\mathcal{E}/2)} \\ &=: f_N(\mathcal{E}/2). \end{aligned} \quad (\text{A5})$$

### 3. Surface of semi-infinite linear chain

The surface Green function of a semi-infinite linear chain can be defined as

$$\begin{aligned} \mathcal{G}_s(\mathcal{E}) &= \lim_{N \rightarrow \infty} [\mathcal{G}^N(\mathcal{E})]_{1,1} \\ &= \lim_{N \rightarrow \infty} f_N(\mathcal{E}/2) \\ &=: f_\infty(\mathcal{E}/2). \end{aligned}$$

To find an expression for  $f_\infty(x)$ , we can use the recursive definition of the Chebyshev polynomials [Eq. (A4)] and

We can now use the well-known identity for the matrix inverse,

obtain

$$f_N(x) = (2x - f_{N-1}(x))^{-1}.$$

For  $N \rightarrow \infty$ , this becomes

$$f_\infty(x) = (2x - f_\infty(x))^{-1},$$

which has two solutions  $f_\infty(x) = x(1 \pm \sqrt{1 - 1/x^2})$ . On the real axis, it follows from Eqn. (A4) by induction that  $|f_N(x)| < 1$  when  $|x| > 1$ , so that we can select the correct solution

$$f_\infty(x) = x(1 - \sqrt{1 - 1/x^2}), \quad (\text{A6})$$

which can be continued analytically to  $x \in \mathbb{C} \setminus (-1, 1)$  by reading the square root of a complex number as the *principal square root*, uniquely defined everywhere except on the negative real axis by the condition  $\text{Re}(\sqrt{x}) \geq 0$ ,  $\forall x \in \mathbb{C}$ .

The retarded surface Green function follows as

$$\begin{aligned} \mathcal{G}_s^r(E) &= \lim_{\eta \rightarrow 0^+} \mathcal{G}_s(E + i\eta) \\ &= \begin{cases} E/2 - \sqrt{E^2/4 - 1} & \text{for } |E| \geq 2 \\ E/2 - i\sqrt{1 - E^2/4} & \text{for } |E| \leq 2 \end{cases} \quad (\text{A7}) \end{aligned}$$

#### 4. Transmission of the model system

With these results, we can now obtain the quantum mechanical transmission of our model system. The left lead is a semi-infinite chain giving a self self-energy of

$$\begin{aligned}\Sigma_L &= H_{cL}(\mathcal{E} - H_L)^{-1} H_{Lc} \\ &= \mathcal{G}_s(\mathcal{E}).\end{aligned}$$

For  $|E| \geq 2$ ,  $\mathcal{G}_s^r(E)$  is real [see Eq. (A7)], so,  $\Gamma_L$  and with it by Eq. (A2) the whole transmission  $T$ , are strictly zero. In the following, we therefore assume  $|E| < 2$  and select the second case in Eq. (A7):

$$\Sigma_L^r = \frac{E}{2} \left( 1 - i\sqrt{4/E^2 - 1} \right)$$

To find the self-energy of the right lead, we use the definition of  $H_R^{\text{eff}}$  from Eq. (A3) and find

$$\begin{aligned}\Sigma_R^r &= H_{cR}(E - H^N + i\Delta/2)^{-1} H_{Rc} \\ &= [\mathcal{G}^N(E + i\Delta/2)]_{1,1} \\ &= f_N(E/2 + i\Delta/4).\end{aligned}$$

Now, we can put together all parts to calculate the transmission,

$$\begin{aligned}\mathcal{G}_c^r &= (E - \Sigma_L^r - \Sigma_R^r)^{-1} \\ &= 2 \left( E + iE\sqrt{4/E^2 - 1} - 2f_N(E/2 + i\Delta/4) \right)^{-1}, \\ \mathcal{G}_c^a &= 2 \left( E - iE\sqrt{4/E^2 - 1} - 2f_N(E/2 - i\Delta/4) \right)^{-1}, \\ \Gamma_L &= i(\Sigma_L^r - \Sigma_L^a) \\ &= E\sqrt{4/E^2 - 1}, \\ \Gamma_R &= i[f_N(E/2 + i\Delta/4) - f_N(E/2 - i\Delta/4)] \\ &= 2\text{Im}[f_N(E/2 - i\Delta/4)] \\ T &= \frac{8\sqrt{4 - E^2} \text{Im}(f_N(E/2 - i\Delta/4))}{|E - i\sqrt{4 - E^2} - 2f_N(E/2 - i\Delta/4)|^2}\end{aligned}\quad (\text{A8})$$

- 
- <sup>1</sup> M. Gheorghe, R. Gutiérrez, N. Ranjan, A. Pecchia, A. D. Carlo, and G. Cuniberti, *Europhys. Lett.* **71**, 438 (2005).
  - <sup>2</sup> D. Mann, A. Javey, J. Kong, Q. Wang, and H. Dai, *Nano Lett.* **3**, 1541 (2003).
  - <sup>3</sup> Z. Yao, C. L. Kane, and C. Dekker, *Phys. Rev. Lett.* **84**, 2941 (2000).
  - <sup>4</sup> A. K. Geim and K. S. Novoselov, *Nat. Mater.* **6**, 183 (2007).
  - <sup>5</sup> H. Schomerus, *Phys. Rev. B* **76**, 045433 (2007).
  - <sup>6</sup> Z. Chen, Y.-M. Lin, M. J. Rooks, and P. Avouris, *Phys. E* **40**, 228 (2007).
  - <sup>7</sup> K. Nakada, M. Fujita, G. Dresselhaus, and M. S. Dresselhaus, *Phys. Rev. B* **54**, 17954 (1996).
  - <sup>8</sup> M. Fujita, K. Wakabayashi, K. Nakada, and K. Kusakabe, *J. Phys. Soc. Jpn.* **65**, 1920 (1996).
  - <sup>9</sup> Y.-W. Son, M. L. Cohen, and S. G. Louie, *Nature (London)* **444**, 347 (2006).
  - <sup>10</sup> M. Wimmer, I. Adagideli, S. Berber, D. Tománek, and K. Richter, (unpublished), 0709.3244.
  - <sup>11</sup> Y. Zhang, N. W. Franklin, R. J. Chen, and H. Dai, *Chem. Phys. Lett.* **331**, 35 (2000).
  - <sup>12</sup> Y. Zhang and H. Dai, *Appl. Phys. Lett.* **77**, 3015 (2000).
  - <sup>13</sup> A. Javey, J. Guo, D. B. Farmer, Q. Wang, D. Wang, R. G. Gordon, M. Lundstrom, and H. Dai, *Nano Lett.* **4**, 447 (2004).
  - <sup>14</sup> B. Shan and K. Cho, *Phys. Rev. Lett.* **94**, 236602 (2005).
  - <sup>15</sup> A. Javey, J. Guo, Q. Wang, M. Lundstrom, and H. Dai, *Nature (London)* **424**, 654 (2003).
  - <sup>16</sup> F. Wakaya, K. Katayama, and K. Gamo, *Microelectron. Eng.* **67-68**, 853 (2003).
  - <sup>17</sup> P.-W. Chiu and S. Roth, *Appl. Phys. Lett.* **91**, 102109 (2007).
  - <sup>18</sup> B. Shan and K. Cho, *Phys. Rev. B* **70**, 233405 (2004).
  - <sup>19</sup> A. Maiti and A. Ricca, *Chem. Phys. Lett.* **395**, 7 (2004).
  - <sup>20</sup> S.-H. Ke, W. Yang, and H. U. Baranger, *J. Chem. Phys.* **124**, 181102 (2006).
  - <sup>21</sup> J. J. Palacios, P. Tarakeshwar, and D. M. Kim, (unpublished), 0705.1328.
  - <sup>22</sup> T. Meng, C.-Y. Wang, and S.-Y. Wang, *J. Appl. Phys.* **102**, 013709 (2007).
  - <sup>23</sup> Y. Liu, *Phys. Rev. B* **68**, 193409 (2003).
  - <sup>24</sup> K. W. Hipps, *Science* **294**, 536 (2001).
  - <sup>25</sup> G. Cuniberti, F. Großmann, and R. Gutiérrez, *Advances in Solid State Physics* **42**, 133 (2002), cond-mat/0209138.
  - <sup>26</sup> N. Nemec, D. Tománek, and G. Cuniberti, *Phys. Rev. Lett.* **96**, 076802 (2006).
  - <sup>27</sup> S. Krompiewski, *Phys. Status Solidi A* **196**, 29 (2003).
  - <sup>28</sup> L. F. Chibotaru, S. Compennolle, and A. Ceulemans, *Phys. Rev. B* **68**, 125412 (2003).
  - <sup>29</sup> I. Deretzis and A. L. Magna, *Nanotechnology* **17**, 5063 (2006).
  - <sup>30</sup> G. Breit and E. P. Wigner, *Phys. Rev.* **49**, 519 (1936).
  - <sup>31</sup> A. D. Stone and P. A. Lee, *Phys. Rev. Lett.* **54**, 1196 (1985).
  - <sup>32</sup> G. García-Calderón, R. Romo, and A. Rubio, *Phys. Rev. B* **47**, 9572 (1993).
  - <sup>33</sup> L. Grüter, F. Cheng, T. T. Heikkilä, M. T. González, F. Diederich, C. Schönenberger, and M. Calame, *Nanotechnology* **16**, 2143 (2005).
  - <sup>34</sup> T. Nakanishi and T. Ando, *J. Phys. Soc. Jpn.* **69**, 2175 (2000).
  - <sup>35</sup> R. M. Corless, G. H. Gonnet, D. E. G. Hare, D. J. Jeffrey, and D. E. Knuth, *Adv. Comput. Math.* **5**, 329 (1996).
  - <sup>36</sup> W. Liang, M. Bockrath, D. Bozovic, J. H. Hafner, M. Tinkham, and H. Park, *Nature (London)* **411**, 665 (2001).
  - <sup>37</sup> J. M. Soler, E. Artacho, J. D. Gale, A. García, J. Junquera, P. Ordejón, and D. Sánchez-Portal, *J. Phys.: Condens. Matter* **14**, 2745 (2002).
  - <sup>38</sup> E. Durgun, S. Dag, V. M. K. Bagci, O. Gülseren, T. Yildirim, and S. Ciraci, *Phys. Rev. B* **67**, 201401 (2003).
  - <sup>39</sup> E. Durgun, S. Dag, S. Ciraci, and O. Gülseren, *J. Phys.*



- Chem. B **108**, 575 (2004).
- <sup>40</sup> D. S. Fisher and P. A. Lee, Phys. Rev. B **23**, 6851 (1981).
- <sup>41</sup> S. Datta, *Electronic Transport in Mesoscopic Systems* (Cambridge University Press, Cambridge, 1999), ISBN 0-521-59943-1.
- <sup>42</sup> I. S. Gradshteyn, I. M. Ryzhik, A. Jeffrey, and D. Zwillinger, *Tables of Integrals, Series, and Products* (Academic Press, San Diego, 2000), 6th ed., ISBN 0-12-294757-6.